Controllable Selective Coupling of Dyakonov Surface Waves at a Liquid-Crystal-Based Interface

Yan Li, Jingbo Sun,* Yongzheng Wen, and Ji Zhou†

State Key Laboratory of New Ceramics and Fine Processing, School of Materials Science and Engineering, Tsinghua University, Beijing 100084, China

(Received 5 June 2019; revised manuscript received 20 December 2019; accepted 8 January 2020; published 11 February 2020)

Highly directional and lossless surface waves have significant potential applications in two-dimensional photonic circuits and devices. Here, we experimentally demonstrate a selective Dyakonov surface wave coupling at the interface between a transparent polycarbonate material and a nematic liquid crystal 5CB. By controlling the anisotropy of the nematic liquid crystal with an applied magnetic field, a single ray at a certain incident angle from a diverged incident beam can be selectively coupled into a surface wave. The implementation of this property may lead to a new generation of on-chip integrated optics and two-dimensional photonic devices.

DOI: 10.1103/PhysRevApplied.13.024024

I. INTRODUCTION

Optical surface waves are special waves of electromagnetic modes strongly confined at the nanoscale, propagating at an interface between two different media [1–3]. Their featured unique physical behaviors, such as surface sensitivity [4–6], field localization [7–9], and tailored interaction with light [10–12], have highlighted their promising applications in sensing [13–15], near-field imaging [16–18], and subwavelength optics [19–21], especially nanoguiding, which can shrink the conventional optical waveguides into two-dimensional photonic circuits [22–25]. The initial way to accomplish a surface mode is to use surface plasmons, which are easy to observe, excited between metal and dielectric media, which is very easy to obtain. Surface plasmons, however, always suffer propagation losses and strong dispersion due to the composition of the metal [26–29]. In contrast, a different type of surface excitation is the so-called Dyakonov surface wave (DSW) [30], which propagates at the interface between two transparent media, at least one of which has to be anisotropic, thus making a lossless surface wave a realistic possibility. Although predicted three decades ago, the DSW was only first observed experimentally in 2009 [31] because of the difficulties of achieving in practice with natural materials the conditions for the correct relationship between the permittivities of the two materials involved; however, on the other hand, this relationship makes the surface wave achieved highly directional. To date, substantial efforts have been invested to achieve the DSW between different interfaces of uniaxial materials [32,33] and biaxial materials [34–36], and even with the help of metamaterials, which can supply a strong anisotropy [37–45], making the realization of DSWs more and more promising. Steering the DSW in a tunable way thus becomes a really desired characteristic but one which has been barely studied so far. Here, we introduce and demonstrate the behavior of DSW coupling at the interface between the nematic liquid crystal (NLC) 5CB and polycarbonate (PC), which, controlled with a magnetic field, exhibits a strongly selective input coupling. NLC can provide a much stronger anisotropy but also a tunability of the orientation that steers the surface-wave coupling magnetically, which allows the potential for developing new types of reconfigurable or switchable devices in photonic circuits that are otherwise difficult or impossible to achieve with conventional technologies.

II. DESIGN

A unique property of the DSW is its highly selective coupling along with its high directional propagation, which is mainly determined by the specific conditions of the isotropic and anisotropic refraction indices at the two sides of the interface; these conditions actually make the DSW hard to observe, but provide a unique method for wave manipulation. As shown in Fig. 1, an interface is formed between an isotropic material with refractive index n_c and a positive uniaxial material with extraordinary refractive index n_e and ordinary refractive index n_o ($n_e > n_o$). With the condition of the materials indices $n_e > n_c > n_o$, the interface can support DSWs propagating with specific wave vectors **K**.

According to Maxwell's equation, the possible direction of **K** is determined with respect to the optical

*jingbosun@tsinghua.edu.cn
†zhouji@tsinghua.edu.cn

 © 2020 American Physical Society

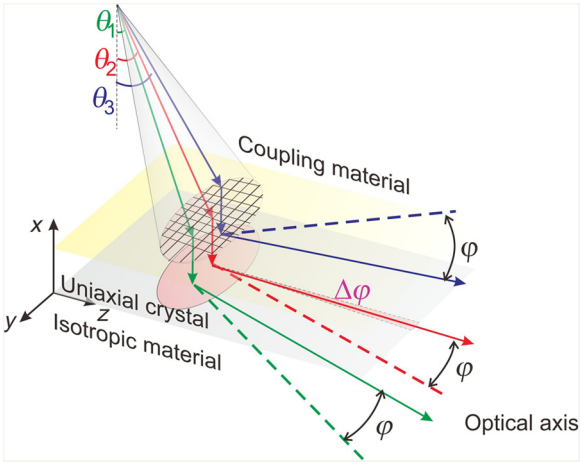

FIG. 1. Selective coupling behavior of a DSW. A diverged beam is incident onto an interface formed by a uniaxial material and an isotropic material. By meshing the illuminating region, the incident beam cone can be considered as a group of rays, each of which has its own identical wave vector and can be potentially coupled into the DSW along the interface as long as the incident wave vector matches the wave vector of the DSW, which is uniquely determined by the orientation of the optical axis in a system of certain materials. To couple the three objective beams, the optical axis is orientated in three different directions so that the angle with respect to the wave vector fulfills the condition Eq. (1).

axis [30]:

$$\sin^2\varphi_{\min} = \frac{\xi}{2}\{1 - \eta\xi + [(1-\eta\xi)^2 + 4\eta]^{1/2}\}, \tag{1a}$$

$$\sin^2\varphi_{\max} = \frac{(1+\eta)^3\xi}{(1+\eta)^2(1+\xi\eta) - \eta^2(1-\xi)^2}, \tag{1b}$$

where $\eta = (n_e^2/n_o^2) - 1$, $\xi = (n_c^2 - n_o^2)/(n_e^2 - n_o^2)$, $\phi_{\min}$ and $\phi_{\max}$ are minimum and maximum allowed angles of DSW.

The modulus of $\mathbf{K} = Nk_0$, expressed as a product of the effective index (N) and the wave vector in the air (k_0), can be determined by solving the transcendental equation [37]

$$\tan^2\varphi = \frac{\gamma_o(\gamma_c + \gamma_o)(n_o^2\gamma_c\gamma_e + n_c^2\gamma_o^2)}{n_o^2(\gamma_c + \gamma_e)(n_o^2\gamma_c + n_c^2\gamma_o)}, \tag{2}$$

where $\gamma_o = \sqrt{N^2 - n_o^2}$, $\gamma_e = \sqrt{N^2[\sin^2\varphi + (n_e^2/n_o^2)\cos^2\varphi] - n_e^2}$, and $\gamma_c = \sqrt{N^2 - n_c^2}$.

Therefore, Eqs. (1) and (2) define the direction and the modulus of the DSW's wave vector at the interface, both of which are determined by the orientation of the optical axis φ.

As shown in Fig. 1, to generate the DSW, the beam with a certain divergence is incident on the interface, which forms a beam cone. By meshing the illumination region, the incident beam can be considered as a group of rays from the source to each joint of the mesh, such as rays 1, 2, 3 in Fig. 1. Each ray has an identical wave vector that is uniquely determined by its incident angle. Inside the incident beam cone, only the ray matching **K** in both modulus and direction can be selectively coupled into the interface as the DSW, which helps us build a strict connection between the orientation angle φ and the incident angle of the ray. Thus, by scanning the optical axis, we can select the matching ray from an incident beam as the input to couple into the DSW and then transport it to the other specific direction at the output.

In order to manipulate the selective coupling, we use a NLC and a transparent PC material to form the tunable interface for the DSW. Under a bias magnetic field, the NLC exhibits a uniaxial positive birefringence as $n_e = 1.6889$ and $n_o = 1.5438$, with its axis aligned along the magnetic field [46]. Therefore, a magnetic field can be used to control the orientation of the optical axis. A PC material with isotropic refractive index of $n_c = 1.5788$ is chosen as the isotropic counterpart, and thus the interface satisfies the condition $n_e > n_c > n_o$, which can be used to excite the DSW [30].

III. EXPERIMENTS

The experimental setup is shown in Fig. 2(a). The s-polarized incident beam (with E field along the y direction) is gently diverged by lens 1 before the modified Otto-Kretchemann configuration. The spot size of the laser beam (DH-HN250P 632.8 nm) is 0.7 mm and the focal length of lens 1 is 150 mm, which makes the beam diverge with an angle $\pm 0.26°$. Mirror 2 is used to induce a small tilt angle ϕ along the y axis. A computer-controlled rotation stage (GCD-011060M) with an angular step size of 0.001°, which can precisely adjust the magnetic field in order to eventually control the orientation of the NLC is set up. The reflected beam after the modified Otto-Kretchemann configuration is firstly collimated by lens 2 and then gently focused by lens 3. A p-polarized analyzer is placed in front of the camera (MER-310-12UC) to filter the beam from the two total reflection regions in order to detect the polarization conversion. In the inset, the whole spot under the s polarization turns into two parts after the p-polarized analyzer (with E field along the z-x plane) because of the polarization conversion.

The modified Otto-Kretchemann configuration consists of a ZnSe prism and a PC block with a layer of the NLC 5CB (Macklin P816665) between. The thickness of the NLC layer is 5.4 μm, which is directly measured by an optical microscope setup, as shown in Fig. 2(b). Such a thickness is around 8.5 λ ($\lambda = 632.8$ nm), which can

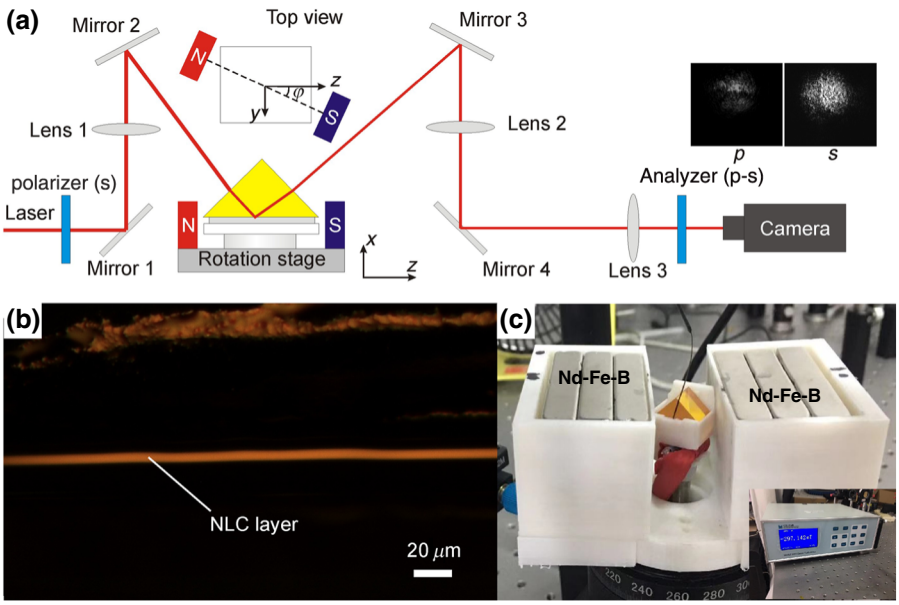

FIG. 2. Experimental setup. (a) Schematic of the setup. The insets show the reflected patterns in the p- (with E field along the z-x plane) and s-polarization states (with E field along the y direction), which produce two spots and one spot, respectively. (b) Optical image of the NLC layer. (c) Otto-Kretchemann configuration placed between a rotating magnetic field supplied by two sets of Nd-Fe-B blocks. The magnetic field is measured to be 297 mT.

provide a proper DSW angle range [31]. The entire Otto-Kretchemann configuration is placed between two sets of Nd-Fe-B blocks, which can supply a magnetic field of 297 mT, measured by a CH-Hall 1600 Gauss-Tesla meter, as shown in Fig. 2(c). The anisotropic refractive indices of the NLC are characterized by a total reflection method under the magnetic field along two orthogonal orientations. The measured n_o and n_e are equal to those measured from an ellipsometer, which means the NLC is fully aligned under the 297-mT magnetic field [47]. Finally, the back surface of the PC block is ground down to form a rough surface to eliminate any possible back reflection from the PC-air interface. The polycarbonate is an optical material used for lenses, which is stable under the exposure of light. For practical applications, the system is encapsulated for the usage of liquid crystal, and therefore the device is isolated from oxygen or humidity resulting in no degradation issues.

IV. RESULTS AND DISCUSSION

A. DSW demonstration

The DSW coupling behavior is demonstrated based on the polarization-conversion reflection scheme (incident-reflected s_{in}-p_{out}) performed in the modified Otto-Kretchemann configuration, where there are three interfaces from the top to the bottom, ZnSe-NLC, NLC-PC, and PC-air, as shown in Fig. 3(a). The refractive index of the ZnSe ($n_{\text{prism}} = 2.5891$) is larger than n_e, and this enables a total reflection when the internal incident angle is larger than the critical angle θ_c at the ZnSe-NLC interface, which creates an evanescent wave coupling into the NLC-PC interface. In our setup, the NLC is sandwiched between the prism and PC. According to Eq. (1), the allowed direction of **K** defined by the angle relative to the optical axis has to be in the range from $\varphi_{\text{min}} = 30.84°$ to $\varphi_{\text{max}} = 31.35°$ ($\Delta\varphi = 0.51°$). By solving Eq. (2), the modulus of **K** can be calculated and, based on Snell's law, we can determine other key parameters, such as the effective index (n_{eff}) of the NLC at φ, the critical angle θ_c, and the internal incident angle (θ_{DSW}) at which the wave vector of the incident ray can match **K**. All the values of these key parameters when φ varies between φ_{min} and φ_{max} are summarized in Table I.

According to Table I, θ_{DSW} is slightly larger than θ_c, which means the DSW coupling always occurs immediately after total reflection. Therefore, in the experiment, the diverged incident beam is adjusted so that its central incident angle is approximately θ_c at the ZnSe-NLC interface. With the divergence, the range of the internal incident angle from θ_{min} to θ_{max} covers both θ_c and θ_{DSW} as $\theta_{\text{min}} < \theta_c \leq \theta_{\text{DSW}} < \theta_{\text{max}}$, and this range can be split into four regions: θ_{min} to θ_c, θ_c to θ_{DSW}, θ_{DSW}, and θ_{DSW} to θ_{max}, corresponding to reflection-refraction, total reflection, reflection-DSW, and total reflection, respectively. Owing to the anisotropy, either the transmission or the evanescent coupling to the DSW is polarization sensitive and may cause a polarization change in the reflected beams, which means part of the s-polarized E field is transformed into p polarization. Such an effect may reach its first maximum when the incident angle is quite close but a little smaller than θ_c and then decline after that [48]. The second maximum appears when the incident angle is equal to θ_{DSW}. If we use a p-polarized analyzer to filter the s polarization (mainly the beams from the total reflection regions) of the reflected beam, we will observe two bright spots, which is a typical image for the existence of the DSW [31]. Here, owing to the scattering of the NLC, the line-shape patterns are expanded into wider spots. One spot appears in the refraction region, which

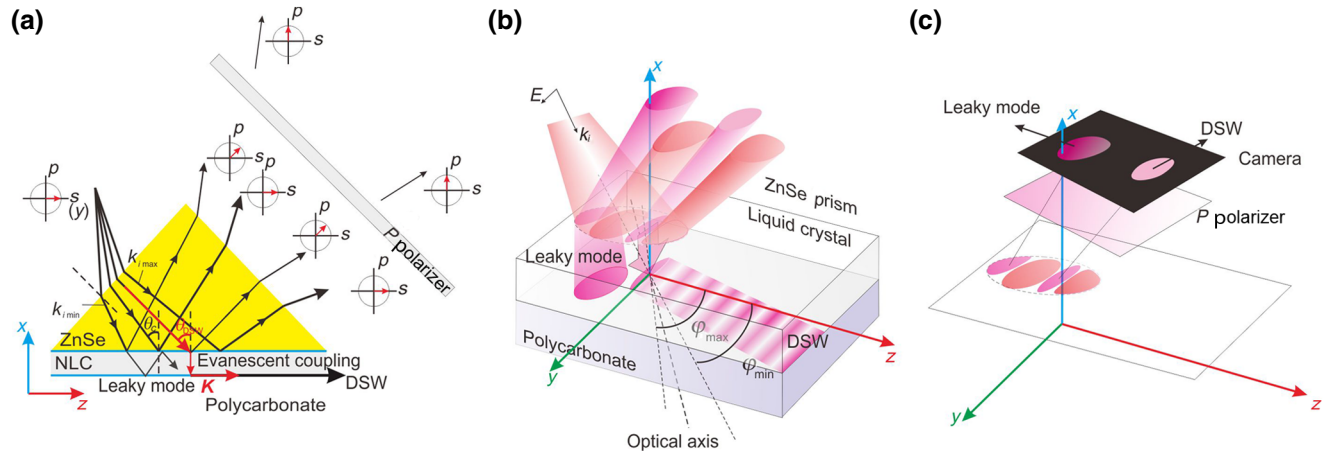

FIG. 3. Schematic of the DSW coupling with a diverged incident beam. (a) Since the divergence contains a series of wave vectors ($k_{i\min}$ to $k_{i\max}$) including the leaky mode and the DSW coupling, the reflection is split into four beams and thus four regions: $\theta_{\min}$ to θ_c, θ_c to θ_{DSW}, θ_{DSW}, and θ_{DSW} to $\theta_{\max}$ with different polarization states. (b) In $\theta_{\min}$ to θ_c, part of the beam transmits through the liquid crystal, which is the leaky mode. At θ_{DSW}, that part of the beam gets coupled into the DSW at the NLC-PC interface. In the other two regions, total reflection occurs. (c) According to polarization conversion theory, after the p polarizer, we can see two bright spots: the leaky mode ($z-$) and the DSW ($z+$). By tracing this pattern back to the ZnSe-NLC interface through the reflected beam, we can see the coupling region changing with the rotation of the optical axis.

is a leaky mode [31], and the other one results from the coupling of the DSW. As shown in Figs. 3(b) and 3(c), along the z direction, the left spot ($z-$) is due to the leaky mode and the right one ($z+$) corresponds to the DSW. This two-spot pattern can be treated as a projection of the p-polarization distribution at the ZnSe-NLC interface in the y-z plane. Therefore, we can demonstrate the selective coupling behavior by analyzing the movement of the DSW spot, where DSW coupling occurs, in the y-z plane while the optical axis is rotating.

B. Select coupling along the z direction

In order to test select coupling along the z direction, we first set the orientation angle of the optical axis to φ with respect to the z axis, as shown in Fig. 4(a). According to Table I, the incident angle is optimized to be 19.4° with a divergence of $\pm 0.26°$ by a lens of $f = 150$ mm, which will finally result in incident angles from $\theta_{\min} = 37.5336°$ to $\theta_{\max} = 37.7247°$ along the z-x plane at the ZnSe-NLC interface. Comparing with $\Delta\varphi$, the divergence in the y direction is small enough ($<\pm 0.1°$) that the y component of the incident wave vector (k_y) can be neglected. Therefore, we only need to consider momentum matching along the z direction. Based on the theoretical prediction in Table I, we precisely control the rotation of the magnetic field from 30.7° to 31.4° and take a photograph of the reflection beam after the p-polarized analyzer by each increase of 0.1°. As shown in Fig. 4(b) at the beginning ($\varphi = 30.7°$), the reflection pattern shows one spot, which means there is no DSW coupling. From 30.8°, two bright spots appear. According to our setup, the highest one is the DSW and it slowly moves toward $z+$ with increase of φ. When φ is 31.4°, the bright spot from the DSW is transformed into a leaky mode. Consequently, only one bright spot appears, which tells us the end of the coupling has been reached. We did not see a second bright spot as predicted in Ref. [31] due to the relatively high loss of the NLC, which attenuated other leaky modes that mainly exist within it. Moreover, the scattering from the NLC expanded the original line-shape pattern into a wider bright spot.

TABLE I. Key parameters in the DSW coupling system.

Name	Parameter	At $\varphi_{\min}$	At $\varphi_{\max}$
Orientation angle (°)	φ	30.84	31.35
Effective index of NLC	n_{eff}	1.5783	1.5793
Critical angle at ZnSe-NLC interface (°)	θ_c	37.5602	37.5881
Wave vector of DSW (**K**)	Nk_0	$1.5788k_0$	$1.5793k_0$
DSW coupling angle at ZnSe-NLC interface (°)	θ_{DSW}	37.5741	37.5881

The movement of the pattern shows a selective coupling behavior along the $z+$ direction, which can be interpreted as follows. First, to ensure that rays in the z-x plane can be coupled, the optical axis is rotating in the range of $\Delta\varphi$ with respect to the z axis. Second, by calculating Eq. (2), the increase of φ results in an increase in value of Nk_0, which requires a larger z component of the wave vector from the incident beam to match, as shown in Fig. 4(a). Thus,

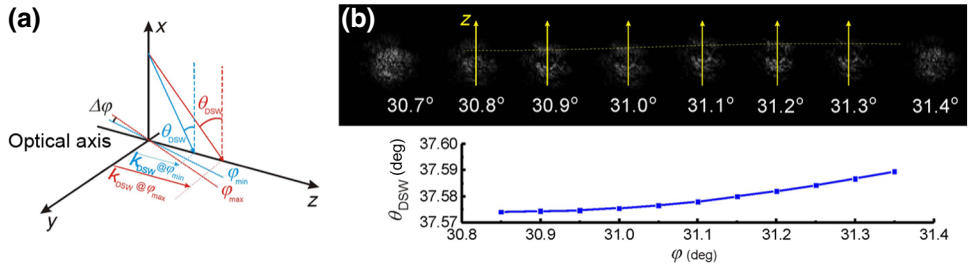

FIG. 4. Selective coupling behavior along the z direction. (a) Schematic of the tunable DSW coupling. When the orientation angle is $\varphi_{\min}$, the blue ray with small θ_{DSW} is coupled into the DSW. When the orientation angle increases to $\varphi_{\max}$, corresponding to a larger Nk_0, the red ray with a larger θ_{DSW} is coupled into the DSW. (b) Observation of the tunable selective DSW coupling in the z-x plane. The orientation angle ranges from 30.7° to 31.4°. The yellow dashed line indicates the upward movement of the spots in the camera. The ray with an incident angle of θ_{DSW} can be coupled into the DSW. The inset shows that θ_{DSW} is rising with an increase of φ.

rays of larger incident angles (θ_{DSW}) in the z-x-plane are coupled into the DSW in sequence, as shown in the inset in Fig. 4(b), which shows the upward movement of the two bright spots. When φ is out of the range 30.8°–31.3°, the direction from the incident cone cannot match **K** and thus no DSW coupling occurs. The one spot is the leaky mode.

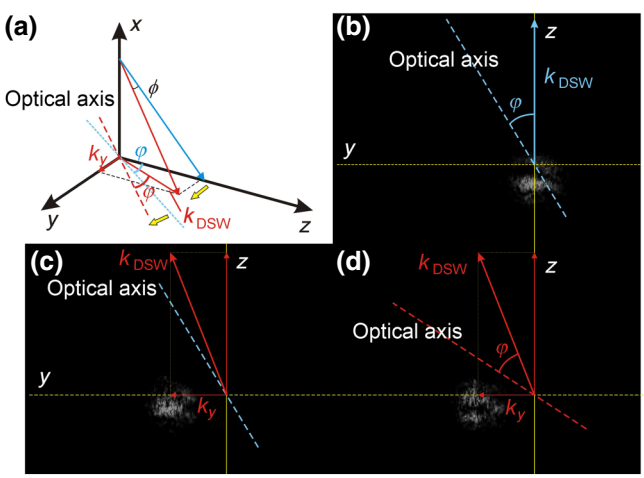

FIG. 5. Selective coupling of the DSW out of the z-x plane. (a) Schematic of the tunable DSW coupling when the incident beam is moving out of the z-x plane by an angle of ϕ. The blue lines indicate the original incidence in the z-x plane and (b) the reflected pattern observed in the camera. The blue dashed line indicates the orientation of the optical axis. The red lines show the incidence with a tilt angle of ϕ and (c) the observed reflected pattern without rotating the magnetic field. The orientation of the optical axis is still the same as that in (b), as labeled by the blue dashed line. (d) By rotating the magnetic field until the angle between the optical axis and the new wave vector is back to φ, the reflected pattern shows two bright spots again. The red dashed line indicates the new orientation of the optical axis. All the orientations of the axes are just schematic and not actual values.

C. Select coupling out of the *z*-*x* plane

Next, we test the selective coupling of the incident beam out of the z-x plane. As we mentioned previously, the beam's own divergence along the y direction is too small to induce k_y, which can affect momentum matching. Therefore, a small tilt angle ϕ is induced between the incident beam and the z-x plane artificially by adjusting a mirror in front of the prism, while φ is set to 31.2°. We carefully increase ϕ until the two original bright spots in Fig. 5(b) start to merge into one from the left-hand side of the pattern, as shown in Fig. 5(c). According to Fig. 5(a), owing to this tilt angle, the wave vector has a component of k_y, which means the actual angle between the new k_{DSW} and the optical axis is less than $\varphi_{\min}$. Thus, there is no coupling of any rays from the incident cone. In order to couple this tilted beam into the DSW, we further rotate the magnetic field so that the optical axis follows the titled beam until φ falls into the range $\varphi_{\min}$ to $\varphi_{\max}$ again. Finally, when we rotate the magnetic field to 33.2°, we can see that one bright spot starts to turn into two bright spots, which means the angle of the optical axis with respect to z falls into the DSW angle range again [as shown in Fig. 5(d)].

Based on the behavior above, we can make a scan over each ray (with its distinguished wave vector) inside the diverged incident beam cone by rotating the optical axis and coupling the expected incident ray as the input to be the DSW.

V. CONCLUSION

In conclusion, we experimentally demonstrate a selective coupling of the DSW at the interface between a transparent PC material and a NLC. By studying the momentum matching condition at the interface, we build a strict connection between the orientation angle φ and the incident angle of the ray. In the experiment, by rotating the optical axis of the NLC with an applied magnetic field, rays with different incident angles from a diverged beam can

be selectively coupled into the surface wave. The selective coupling property along with the highly directional lossless propagation of the DSW can be used to manipulate both the input and the output of a surface-wave system simultaneously, which can be readily integrated on a chip to form ultracompact switchable devices.

ACKNOWLEDGMENTS

This work was supported by the Basic Science Center Project of NSFC under Grant No. 51788104, and the National Natural Science Foundation of China under Grants No. 51532004, No. 11704216, and No. 11974203.

[1] O. Takayama, A. A. Bogdanov, and A. V. Lavrinenko, Photonic surface waves on metamaterial interfaces, J. Phys.: Condens. Matter. **29**, 463001 (2017).

[2] A. J. Polo, Jr., and A. Lakhtakia, Surface electromagnetic waves: A review, Laser Photon. Rev. **5**, 234 (2011).

[3] P. Yeh, A. Yariv, and A. Y. Cho, Optical surface waves in periodic layered media, Appl. Phys. Lett. **32**, 104 (1978).

[4] S. Zhang, K. Bao, N. J. Halas, H. Xu, and P. Nordlander, Substrate-induced Fano resonances of a plasmonic nanocube: A route to increased-sensitivity localized surface plasmon resonance sensors revealed, Nano Lett. **11**, 1657 (2011).

[5] J. Lin, J. B. Mueller, Q. Wang, G. Yuan, N. Antoniou, X. C. Yuan, and F. Capasso, Polarization-controlled tunable directional coupling of surface plasmon polaritons, Science **340**, 331 (2013).

[6] R. Zia and M. L. Brongersma, Surface plasmon polariton analogue to Young's double-slit experiment, Nat. Nanotechnol. **2**, 426 (2007).

[7] L. J. Sherry, S. H. Chang, G. C. Schatz, R. P. Van Duyne, B. J. Wiley, and Y. Xia, Localized surface plasmon resonance spectroscopy of single silver nanocubes, Nano Lett. **5**, 2034 (2005).

[8] S. A. Maier and H. A. Atwater, Plasmonics: Localization and guiding of electromagnetic energy in metal/dielectric structures, J. Appl. Phys. **98**, 011101 (2005).

[9] T. P. Sidiropoulos, R. Röder, S. Geburt, O. Hess, S. A. Maier, C. Ronning, and R. F. Oulton, Ultrafast plasmonic nanowire lasers near the surface plasmon frequency, Nat. Phys. **10**, 870 (2014).

[10] M. L. Liz-Marzán, Tailoring surface plasmons through the morphology and assembly of metal nanoparticles, Langmuir **22**, 32 (2006).

[11] T. J. Echtermeyer, S. Milana, U. Sassi, A. Eiden, M. Wu, E. Lidorikis, and A. C. Ferrari, Surface plasmon polariton graphene photodetectors, Nano Lett. **16**, 8 (2015).

[12] S. A. Maier, S. R. Andrews, L. Martin-Moreno, and F. J. Garcia-Vidal, Terahertz Surface Plasmon-Polariton Propagation and Focusing on Periodically Corrugated Metal Wires, Phys. Rev. Lett. **97**, 176805 (2006).

[13] M. N. Alam, R. H. Bhuiyan, R. A. Dougal, and M. Ali, Design and application of surface wave sensors for nonintrusive power line fault detection, IEEE Sens. J. **13**, 339 (2012).

[14] J. Homola, S. S. Yee, and G. Gauglitz, Surface plasmon resonance sensors, Sens. Actuator B-Chem **54**, 3 (1999).

[15] P. Berini, Long-range surface plasmon polaritons, Adv. Opt. Photonics **1**, 484 (2009).

[16] K. Ishihara, K. Ohashi, T. Ikari, H. Minamide, H. Yokoyama, J. I. Shikata, and H. Ito, Terahertz-wave near-field imaging with subwavelength resolution using surface-wave-assisted bow-tie aperture, Appl. Phys. Lett. **89**, 201120 (2006).

[17] D. K. Gramotnev and S. I. Bozhevolnyi, Plasmonics beyond the diffraction limit, Nat. Photonics **4**, 83 (2010).

[18] L. U. C. A. Piazza, T. T. A. Lummen, E. Quinonez, Y. Murooka, B. W. Reed, B. Barwick, and F. Carbone, Simultaneous observation of the quantization and the interference pattern of a plasmonic near-field, Nat. Commun. **6**, 6407 (2015).

[19] W. L. Barnes, A. Dereux, and T. W. Ebbesen, Surface plasmon subwavelength optics, Nature **424**, 824 (2003).

[20] A. V. Zayats, I. I. Smolyaninov, and A. A. Maradudin, Nano-optics of surface plasmon polaritons, Phys. Rep. **408**, 131 (2005).

[21] S. I. Bozhevolnyi, V. S. Volkov, E. Devaux, J. Y. Laluet, and T. W. Ebbesen, Channel plasmon subwavelength waveguide components including interferometers and ring resonators, Nature **440**, 508 (2006).

[22] C. Ropers, C. C. Neacsu, T. Elsaesser, M. Albrecht, M. B. Raschke, and C. Lienau, Grating-coupling of surface plasmons onto metallic tips: A nanoconfined light source, Nano Lett. **7**, 2784 (2007).

[23] A. A. High, R. C. Devlin, A. Dibos, M. Polking, D. S. Wild, J. Perczel, and H. Park, Visible-frequency hyperbolic metasurface, Nature **522**, 192 (2015).

[24] J. Sun, and N. M. Litchinitser, *Fundamental and Applications of Nanophotonics* (Woodhead Pub., Cambridge, 2016), Chapter 9, pp. 235–307.

[25] A. V. Kildishev, A. Boltasseva, and V. M. Shalaev, Planar photonics with metasurfaces, Science **339**, 1232009 (2013).

[26] S. Sun, H. T. Chen, W. J. Zheng, and G. Y. Guo, Dispersion relation, propagation length and mode conversion of surface plasmon polaritons in silver double-nanowire systems, Opt. Express **21**, 14591 (2013).

[27] J. A. Dionne, L. A. Sweatlock, H. A. Atwater, and A. Polman, Planar metal plasmon waveguides: Frequency-dependent dispersion, propagation, localization, and loss beyond the free electron model, Phys. Rev. B **72**, 075405 (2005).

[28] J. M. Pitarke, V. M. Silkin, E. V. Chulkov, and P. M. Echenique, Theory of surface plasmons and surface-plasmon polaritons, Rep. Prog. Phys. **70**, 1 (2006).

[29] M. Bernardi, J. Mustafa, J. B. Neaton, and S. G. Louie, Theory and computation of hot carriers generated by surface plasmon polaritons in noble metals, Nat. Commun. **6**, 7044 (2015).

[30] M. I. Dyakonov, New type of electromagnetic wave propagating at an interface, Sov. Phys. JETP **67**, 714 (1988).

[31] O. Takayama, L.-C. Crasovan, D. Artigas, and L. Torner, Observation of Dyakonov Surface Waves, Phys. Rev. Lett. **102**, 043903 (2009).

[32] O. Takayama, P. Dmitriev, E. Shkondin, O. Yermakov, M. Panah, K. Golenitskii, and A. Lavrinenko, Experimental observation of Dyakonov plasmons in the mid-infrared, Semiconductors **52**, 442 (2018).

[33] O. Takayama, E. Shkondin, A. Bodganov, M. E. Aryaee Panah, K. Golenitskii, P. Dmitriev, and A. V. Lavrinenko, Midinfrared surface waves on a high aspect ratio nanotrench platform, ACS Photonics **4**, 2899 (2017).

[34] O. Takayama, L.-C. Crasovan, D. Artigas, and L. Torner, Lossless directional guiding of light in dielectric nanosheets using Dyakonov surface waves, Nat. Nanotechnol. **9**, 419 (2014).

[35] L. Torner, J. P. Torres, and D. Mihalache, New type of guided waves in birefringent media, IEEE Photonics Technol. Lett. **5**, 201 (1993).

[36] O. Takayama, A. Y. Nikitin, L. Martin-Moreno, L. Torner, and D. Artigas, Dyakonov surface wave resonant transmission, Opt. Express **19**, 6339 (2011).

[37] D. Artigas and L. Torner, Dyakonov Surface Waves in Photonic Metamaterials, Phys. Rev. Lett. **94**, 013901 (2005).

[38] O. Takayama, L. C. Crasovan, S. K. Johansen, D. Mihalache, D. Artigas, and L. Torner, Dyakonov surface waves: A review, Electromagnetics **28**, 126 (2008).

[39] E. Cojocaru, Comparative analysis of Dyakonov hybrid surface waves at dielectric–elliptic and dielectric–hyperbolic media interfaces, J. Opt. Soc. Am. B **31**, 2558 (2014).

[40] L. Torner, F. Canal, and J. Hernandez-Marco, Leaky modes in multilayer uniaxial optical waveguides, Appl. Optics **29**, 2805 (1990).

[41] O. Takayama, D. Artigas, and L. Torner, Coupling plasmons and Dyakonons, Opt. Lett. **37**, 1983 (2012).

[42] T. Matsui, Dyakonov surface waves in nanoparticle-dispersed liquid crystal metamaterials, Appl. Phys. Express **8**, 072601 (2015).

[43] C. J. Zapata-Rodríguez, J. J. Miret, S. Vuković, and M. R. Belić, Engineered surface waves in hyperbolic metamaterials, Opt. Express **21**, 19113 (2013).

[44] M. Moradi and A. R. Niknam, Terahertz Dyakonov surface waves in plasma metamaterials, Opt. Lett. **43**, 519 (2018).

[45] M. Moradi and A. R. Niknam, Terahertz Dyakonov plasmon surface waves supported by a plasma/TiO_2 interface, Phys. Rev. B **98**, 085403 (2018).

[46] G. Abbate, V. Tkachenko, A. Marino, F. Vita, M. Giocondo, A. Mazzulla, and L. De Stefano, Optical characterization of liquid crystals by combined ellipsometry and half-leaky guided-mode spectroscopy in the visible-near infrared range, J. Appl. Phys. **101**, 073105 (2007).

[47] J. Gao, R. Wang, Q. Zhao, B. Li, and J. Zhou, A modularized and switchable component for flexible passive device: Terahertz photonic crystals with fine-tuning, Adv. Opt. Mater. **19**, 1800384 (2018).

[48] F. Yang and J. R. Sambles, Critical angles for reflectivity at an isotropic-anisotropic boundary, J. Mod. Opt. **40**, 1131 (1993).